PHYSICAL REVIEW B **106**, 214519 (2022)

Angle-resolved resistivity method for precise measurements of electronic nematicity

Gangfan Chen,[1,2] Yichi Zhang,[1,2] Zhaoguogang Leng,[2,3] Guangyu Xi,[1,2] Wei Zhu,[2] and Jie Wu[2,*]

[1]*Department of Physics, Zhejiang University, Hangzhou 310027, China*
[2]*Key Laboratory for Quantum Materials of Zhejiang Province, School of Science, Westlake University, Hangzhou 310024, China*
[3]*Department of Physics, Fudan University, Shanghai 200433, China*

(Received 9 August 2022; accepted 8 December 2022; published 21 December 2022)

Electronic nematicity is an intriguing phenomenon found in unconventional superconductors and its mechanism invokes intense studies. The precise measurement of the director and amplitude of electronic nematicity by electric transport demands a full mapping of the longitudinal and transverse resistivity, ρ and ρ_T, along different directions. Fabricating Hall bars along every possible in-plane direction would be so labor intensive and vulnerable to sample to sample variations that it becomes impractical. Instead, here we make the local current density $\boldsymbol{J}$ continuously rotate in plane by independently controlling its in-plane components along two orthogonal axes and measure ρ and ρ_T as a function of the azimuth angle ϕ between $\boldsymbol{J}$ and the crystallographic [100] direction. Clear substantial angular oscillations in $\rho(\phi)$ and $\rho_T(\phi)$ were observed from the optimally doped $La_{1.84}Sr_{0.16}CuO_4$ film, in stark contrast to those of the control gold film. This angle-resolved resistivity method demonstrates unprecedented precision in determining the director and amplitude of electronic nematicity and is applicable to anisotropic transport due to mechanisms other than electronic nematicity as well. This method paves the way for the studies of the nematic domains and fluctuations of the nematic order in films and bulk crystals.

DOI: 10.1103/PhysRevB.106.214519

I. INTRODUCTION

Electronic nematicity [1–3] has been found in several important classes of unconventional superconductors, including cuprate [4–15], ruthenate [16,17], Fe-based [18–20] and heavy-Fermion superconductors [21], and superconducting magic-angle graphene [22]. It is illustrated that high-temperature superconductivity in fact emerges out of the electronic nematic state [8]. The underlying mechanism for the breaking of rotational symmetry is an intriguing unresolved question and its connection with the unconventional superconductivity invokes in-depth studies.

With this initiative, a couple of experimental techniques have been employed to probe the electronic nematicity, such as electrical transport [6–10,16,17,21], Nernst effect [11], scanning tunneling microscopy and spectroscopy [12], angle-resolved photoemission spectroscopy [4,5], linear dichroism of THz optics [13,14], etc. Among them, electrical transport is most convenient and widely used for its simplicity and affordability in experimental setups. Nevertheless, the conventional ways, such as the Montgomery method [23], to measure the anisotropic transport by measuring the longitudinal resistivity along two orthogonal crystallographic orientations, e.g., [100] and [010], is sufficient to determine the director and the amplitude of electronic nematicity only when the director of the nematicity is aligned with the crystal lattice. This condition, however, is generally not satisfied since electronic nematicity is engendered by the electron-electron correlation, different from the anisotropy induced by lattice distortions. As shown in $La_{2-x}Sr_xCuO_4$ (LSCO) superconductors, the director of electronic nematicity varies with chemical doping and temperature and in most cases is not aligned with the lattice [8]. Thus, a precise measurement of both the director and the amplitude of the nematicity demands a full mapping of transport along all directions.

Towards this goal, Wu *et al.* conceived and implemented an angle-resolved method to measure the longitudinal resistivity ρ and transverse resistivity ρ_T [8]. A Hall bar with gold contacts attached was fabricated by UV photolithography, from which ρ and ρ_T can be measured simultaneously. Then such a Hall bar was repeated 35 times along systematically varying in-plane directions to form a “sun-beam” pattern with a 10° difference between the successive bars. The angular dependence of ρ and ρ_T measured in this way was shown to be effective in determining the director and amplitude of the electronic nematicity with an angular resolution of 10°. However, due to the inhomogeneity caused by sample growth and device fabrication, the induced random variations in ρ and ρ_T from one Hall bar to another are comparable to the signals of electronic nematicity, making it hard to probe the real signal. For instance, the angular oscillations in ρ for optimally and overdoped LSCO is smeared out by the random variations [8] when the nematicity amplitude of these dopings is less than 3%. The limited angular resolution and sensitivity restricts studies on electronic nematicity.

By virtue of this method, in this paper we developed a more efficient, reliable, and precise method to measure electronic nematicity. The key of the previous method, which is to vary the current direction in plane, was realized by fabricating Hall bars with different orientations that guide the direction of the current running along them. However, this can be

---

[*] wujie@westlake.edu.cn

accomplished in an alternative but neater way by taking advantage of the vector property of the current density $\boldsymbol{J}$. The direction of the vector $\boldsymbol{J}$ can be effectively rotated in plane continuously from $\phi = 0^\circ$ to 360° by independently controlling its $\boldsymbol{x}$ and $\boldsymbol{y}$ components $\boldsymbol{J}_x$ and $\boldsymbol{J}_y$. Here ϕ is the angle $\boldsymbol{J}$ makes with the $\boldsymbol{x}$ axis. Then we can measure $\rho(\phi)$ and $\rho_T(\phi)$ without the need of fabricating massive numbers of devices, greatly reducing the influence due to inhomogeneity in film growth and device fabrication that is the biggest hurdle to the improvement of the sensitivity of electronic nematicity measurement. The angular resolution of the nematic director is determined by the angle interval $\Delta\phi$ that was limited only by the precision in the output of $\boldsymbol{J_x}$ and $\boldsymbol{J_y}$ so it can easily reach the millidegree level, at least four orders of magnitude higher than the previous method.

This angle-resolved resistivity (ARR) method by independently tuning $\boldsymbol{J_x}$ and $\boldsymbol{J_y}$ is applicable to research not limited to electronic nematicity. Anisotropic transport due to other mechanisms, e.g., anisotropic magnetoresistance [24], directional superconducting vortex motion [25], or intentionally introduced anisotropy [26], can be measured following the same scheme. Therefore, in general ARR is a high-resolution high-precision method to measure the resistivity tensor.

To illustrate the effectiveness of the ARR method, we chose an optimally doped LSCO ($x = 0.16$) thin film as the test sample and a common metal, Au, as a control sample. Optimally doped LSCO films are electronic nematic and as the temperature lowers from room temperature and approaches the superconducting temperature T_c, the director of the nematicity rotates significantly [8]—an ideal test system for our purpose. The gold sample, on the other hand, is not nematic so the anisotropy in its transport, if any, should be of extrinsic origin, e.g., variations in film thickness, imperfections in lithography process, etc., so its amplitude should be relatively small under well-controlled experimental conditions. By contrasting the results from LSCO and gold films, we can unambiguously single out the signals from electronic nematicity and determine the sensitivity of the ARR method.

II. METHODS

LSCO ($x = 0.16$) films were grown by pulsed laser deposition (PLD) onto LaSrAlO$_4$(001) substrates. Prior to deposition, the substrate was annealed at 670 °C for 20 min under 1×10^{-2} Torr oxygen pressure until a very sharp reflection high-energy electron diffraction (RHEED) pattern emerged. During growth, the substrate temperature was kept at 650 °C and the oxygen pressure was 8.5×10^{-2} Torr. The laser energy was set to 1 J/cm^2 and the frequency of laser pulses was 2 Hz. The growth process was monitored by *in situ* RHEED and a good layer by layer growth mode was verified by the oscillations in intensity of RHEED spots during growth. The postgrowth LSCO film was kept at 400 °C for 40 min in 3.8×10^2 Torr oxygen pressure to reduce the amount of oxygen vacancies. As the result of continuous optimizations of growth, these growth parameters give the best quality films with our setup. *Ex situ* x-ray diffraction spectroscopy confirms the high crystallinity of the 26 nm LSCO film (equivalent to 20 unit cell thickness). Atomic force microscopy shows the rms roughness of the LSCO film is 0.6 nm, smaller than its c-axis lattice constant 1.32 nm, confirming the film is atomically flat. Meanwhile, the control sample, a 10 nm gold film, was deposited onto a MgO(001) substrate by magnetron sputtering. The MgO(001) substrate was kept at room temperature during deposition. For transport measurements, dc currents are generated by Keithley 2450 sourcemeters and dc voltages are measured by Keithley 2182A nanovoltmeters. The samples are mounted onto a cryocooler for temperatures to be varied between 300 and 4 K.

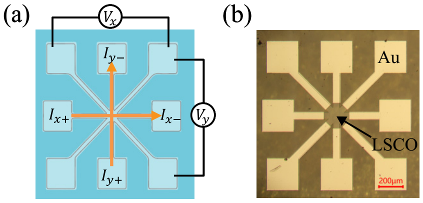

FIG. 1. (a) The lithography pattern for the ARR method. The current I_x and I_y are independently controlled in such a way that the net current density $\boldsymbol{J}$ at the cross section rotates its direction in plane while maintaining a constant magnitude. The $\boldsymbol{x}$ axis is chosen to be parallel to the [100] direction of the LSCO lattice and the angle ϕ between $\boldsymbol{J}$ and $\boldsymbol{x}$ is varied from 0° to 360°. The resistivity tensor is determined by measuring the voltages V_x and V_y as a function of ϕ. (b) The photo of a patterned LSCO film. The contact pads and bars are covered by a 100 nm thick gold layer for better electric contact.

The LSCO films were patterned by standard UV lithography to form the devices shown in Figs. 1(a) and 1(b). $\boldsymbol{J_x}$ and $\boldsymbol{J_y}$ at the cross section of the device are independently controlled by the currents injected from I_x+, I_x- and I_y+, I_y- contacts, respectively. By letting $I_x = I_0\sin\phi$ and $I_y = I_0\cos\phi$, we can make the net $\boldsymbol{J}$ at the cross section to rotate in plane at any desired interval $\Delta\phi$, covering the complete range from $\phi = 0^\circ$ to 360°. In the LSCO film, ϕ denotes the angle between $\boldsymbol{J}$ and the [100] direction of the LSCO lattice. Meanwhile, the voltages V_x and V_y measured along the $\boldsymbol{x}$ and $\boldsymbol{y}$ axes can be decomposed to components parallel and transverse to $\boldsymbol{J}$. Then the longitudinal voltage in the direction of $\boldsymbol{J}$ is $V_L = V_x\sin\phi + V_y\cos\phi$ and the voltage transverse to $\boldsymbol{J}$ is $V_T = V_x\cos\phi - V_y\sin\phi$. For the control gold film, the patterning and measurements were done in exactly the same way except that ϕ there is the angle between $\boldsymbol{J}$ and the [100] direction of the MgO(001) substrate.

III. RESULTS AND DISCUSSION

Figure 2 shows the angle-dependent longitudinal and transverse resistivity $\rho(\phi)$ and $\rho_T(\phi)$ of the gold and LSCO sample at room temperature. Very small modulations on both the longitudinal and transverse resistivity are visible for the gold film. Its magnitude, $\Delta\rho/\bar{\rho} \sim 0.09\%$ is 40 times smaller than $\Delta\rho/\bar{\rho}$ of the LSCO film (~3.6% at room temperature), where $\Delta\rho$ is the amplitude of the angular oscillation in longitudinal resistivity and $\bar{\rho}$ is the angle-averaged longitudinal resistivity. We have synthesized a couple of gold thin films under exactly the same conditions and found that this small anisotropy is sample dependent and presumably is related with the variation in film thickness at macroscopic scale. It is experimentally challenging to make the film uniformity reach the level of 0.09% so when we have a very sensitive probe, such as the

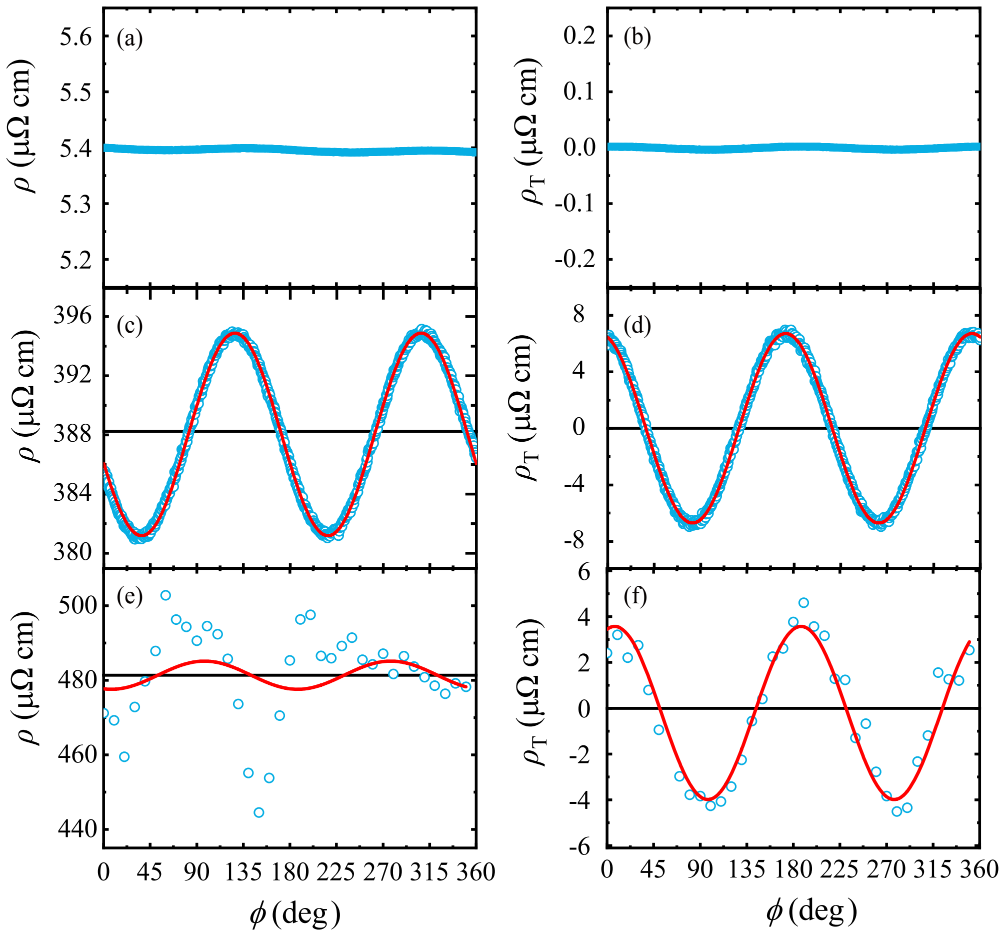

FIG. 2. (a) The longitudinal resistivity $\rho(\phi)$ and (b) the transverse resistivity $\rho_T(\phi)$ of the gold film, the control sample, measured at room temperature. Both manifest very little angular dependence and $\rho_T(\phi)$ is tiny for all ϕ. (c), (d), $\rho(\phi)$ and $\rho_T(\phi)$ of the LSCO ($x = 0.16$) film measured at room temperature. In stark contrast to the gold film, $\rho(\phi)$ and $\rho_T(\phi)$ of LSCO show significant angular oscillations that can be well fitted by Eqs. (1) and (2). The blue circles are experimental data and the solid red curves are fitted curves. Their agreements are remarkable. (e), (f), $\rho(\phi)$ and $\rho_T(\phi)$ of the LSCO ($x = 0.16$) film measured by the sunbeam method [8] are shown as a comparison. Obviously, the random angle to angle variations are much smaller in (c), (d) than (e), (f).

ARR method, we can pick up a tiny signal that used to be buried under experimental noise. In stark contrast to the gold film, $\rho(\phi)$ and $\rho_T(\phi)$ of the LSCO film show correlated substantial angular oscillations in ϕ with a period of 180°, which is a direct consequence of the broken rotational symmetry in the presence of the electronic nematicity.

For anisotropic in-plane transport, the resistivity tensor takes the form of a rank-2 tensor:

$$\rho = \begin{pmatrix} \rho_a & 0 \\ 0 & \rho_b \end{pmatrix}.$$

Here $\boldsymbol{e}_a$ and $\boldsymbol{e}_b$ are the principal axes.

If the axes are rotated by an angle ϕ so that $\boldsymbol{e}_x = \hat{C}_\phi \boldsymbol{e}_a$ and $\boldsymbol{e}_y = \hat{C}_\phi \boldsymbol{e}_b$, in the $\boldsymbol{e}_x$ and $\boldsymbol{e}_y$ coordinate system, the resistivity tensor becomes

$$\hat{C}_\phi \rho \hat{C}_\phi^{-1} = \begin{pmatrix} \cos\phi & -\sin\phi \\ \sin\phi & \cos\phi \end{pmatrix} \begin{pmatrix} \rho_a & 0 \\ 0 & \rho_b \end{pmatrix} \begin{pmatrix} \cos\phi & \sin\phi \\ -\sin\phi & \cos\phi \end{pmatrix}$$

$$= \begin{pmatrix} \bar{\rho} + \Delta\rho\cos(2\phi) & \Delta\rho\sin(2\phi) \\ \Delta\rho\sin(2\phi) & \bar{\rho} - \Delta\rho\cos(2\phi) \end{pmatrix}.$$

Here $\bar{\rho} = (\rho_a + \rho_b)/2$ and $\Delta\rho = (\rho_a - \rho_b)/2$.

Taking into consideration that in general the principal axes $\boldsymbol{e}_a$ and $\boldsymbol{e}_b$ are not aligned with the crystallographic [100] and [010] directions, let us denote the angle between $\boldsymbol{e}_a$ and [100] as α. Therefore, the angular dependence of $\rho(\phi)$ and $\rho_T(\phi)$ for anisotropic electrical transport conform to the following relations [8]:

$$\rho_T(\phi) = \Delta\rho\sin[2(\phi - \alpha)], \tag{1}$$

$$\rho(\phi) = \bar{\rho} + \Delta\rho\cos[2(\phi - \alpha)]. \tag{2}$$

The amplitude and the phase offset of the angular oscillations, $\Delta\rho$ and α, are directly related with the amplitude and director of the electronic nematicity under study.

The measured $\rho(\phi)$ and $\rho_T(\phi)$ [blue circles in Figs. 2(c) and 2(d)] are well fitted by the expressions (1) and (2) [red solid line in Figs. 2(c) and 2(d)]. Note that the same set of fitting parameters, $\Delta\rho$ and α, works for both $\rho(\phi)$ and $\rho_T(\phi)$, illustrating $\rho(\phi)$ and $\rho_T(\phi)$ are strongly correlated and $\rho_T(\phi)$ indeed is the product of anisotropic $\rho(\phi)$. More importantly, the deviations between experimental data and theoretical curves are remarkably small. To give a direct comparison, $\rho(\phi)$ and $\rho_T(\phi)$ measured by the sunbeam method

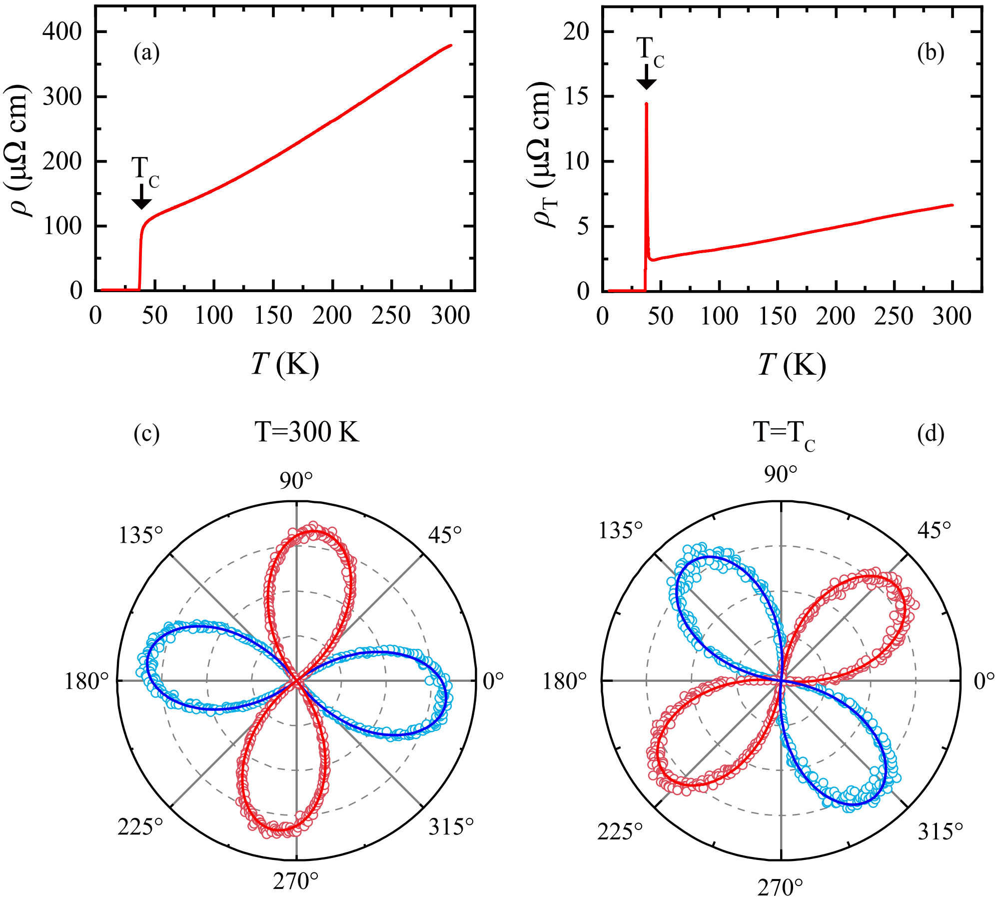

FIG. 3. (a) $\rho(T)$ of LSCO ($x = 0.16$) sample for $\phi = 0°$. The superconducting T_c, defined as the middle point of the resistivity drop, is around 37.5 K. (b) $\rho_T(T)$ for $\phi = 0°$. A pronounced peak in $\rho_T(T)$ at T_c shows the nematic amplitude is greatly enhanced by the superconducting fluctuations, in agreement with Ref. [8]. (c) $\rho_T(\phi)$ at $T = 300\,\mathrm{K}$ plotted in the polar coordinates. The open circles are experimental data and the solid curve is the best fitting using Eq. (2). Blue denotes positive value and red denotes negative. (d) $\rho_T(\phi)$ taken at T_c. A clear reorientation of the nematic director is evident by the comparison between (c) and (d).

on a molecular beam epitaxy (MBE)-grown LSCO film with the same doping are shown in Figs. 2(e) and 2(f) (data were reproduced from Ref. [8]).

Despite the drastic differences in film growth (PLD versus molecular beam epitaxy), lithography patterning [Fig. 1(b) versus sunbeam pattern], and transport measurement (rotating $\boldsymbol{J}$ by tuning its $\boldsymbol{x}$ and $\boldsymbol{y}$ components versus by flowing currents along Hall bars with different directions), $\rho(\phi)$ and $\rho_T(\phi)$ in Fig. 2 reach remarkable agreement. The consistency between two independent methods rules out the possibility that the angular oscillations in $\rho(\phi)$ and $\rho_T(\phi)$ are due to artifacts related with film growth, lithography, or measurements, thus confirming the nematic state is intrinsic to LSCO films. Optical studies on LSCO and YBCO films [14] showed very similar angular dependence of nonlinear optical effects, corroborating that the electronic nematicity would manifest itself in different properties of materials, e.g., electric transport, optics, etc.

The random angle to angle variations in $\rho(\phi)$ and $\rho_T(\phi)$ are significantly reduced by the ARR method when comparing Figs. 2(c) and 2(d) with Figs. 2(e) and 2(f). The resultant improvement in the precision of the ARR method is due to the fact that the $\rho(\phi)$ and $\rho_T(\phi)$ by the ARR method are measured on a single device by rotating the $\boldsymbol{J}$ vector in plane, so it greatly reduces the influence of inhomogeneity in film growth and random variations in device fabrication, which is the main source of the variations for the sunbeam method with 36 devices fabricated and measured. The angular resolution of the sunbeam method is 10° while that of the ARR method currently reaches 0.1°. The resolution of the ARR method is only limited by the noise floor in voltage measurement and can easily be further improved to 0.01° and better if necessary. Therefore, the enhanced precision of the ARR method enabled us to determine the electronic nematicity with unprecedented accuracy.

The symmetry of $\rho(\phi)$ and $\rho_T(\phi)$ can be better illustrated by plotting them in the polar coordinates (Fig. 3). $\rho(\phi)$ shows a dumbbell shape and $\rho_T(\phi)$ shows a cloverleaf shape. Both have a period of 180° that corresponds to the $\boldsymbol{C}_2$ symmetry. It should be emphasized that the LSCO film was epitaxially grown onto the LSAO substrate so the lattice of LSCO was pinned to be tetragonal by the underneath tetragonal LSAO lattice, as verified by x-ray diffraction (XRD) spectroscopy [8]. That means, the lattice of LSCO possesses a $\boldsymbol{C}_4$ symmetry while the electrical transport of LSCO has a lower $\boldsymbol{C}_2$ symmetry, indicating the origin of the anisotropic transport is purely electronic. Strictly speaking, due to the electron-lattice coupling, a tiny lattice distortion below the sensitivity of the XRD method may take place but it is, at best, of secondary importance and cannot be the source of the nematicity in LSCO films. Moreover, as the temperature was lowered from room temperature to the superconducting temperature T_c, the director of the electronic nematicity rotated by as much as 45°, in good agreement with previous findings [8]. The rotation of the nematic director indicated the anisotropic transport in the presence of the superconducting fluctuations bears a different orientation from that of the normal state of LSCO. In other words, the superconducting fluctuations are nematic as well. Plausibly, this is related with the superconducting mechanism of copper oxide superconductors and certainly invokes in-depth studies, which is outside of this paper's scope. Nevertheless, here we provide a very sensitive and precise method that would be a powerful tool apt for such intriguing topics.

For conventional methods, such as the Montgomery method, the misalignment of contacts is a source of error that causes a mixture of ρ with ρ_T. However, its influence on the precision of the ARR method is negligibly small as we show below. The precision of the contact alignment by the lithography process we employed is better than 1 μm and that restricts $\rho_T^*/\rho < 1\%$ (ρ_T^* denotes the transverse resistivity generated by the contact misalignment), given the dimensions of the lithography pattern shown in Fig. 1. Moreover, the ratio ρ_T^*/ρ depends only on geometric factors so it should be independent of the temperature, which is contrary to Figs. 3(a) and 3(b). Also, ρ_T^* should have the same angular dependence as $\rho(\phi)$. In contrast, ρ_T from the nematicity should have a 45° phase shift compared to $\rho(\phi)$ according to the expressions (1) and (2) in the paper. The weight of these two contributions can be extracted from the overall phase shift between $\rho(\phi)$ and $\rho_T(\phi)$. For both room temperature and T_c, the phase shift from the best fittings of $\rho(\phi)$ and $\rho_T(\phi)$ is exactly 45°, proving ρ_T^* is negligibly small.

The sunbeam pattern takes up 10 mm × 10 mm in space and demands the sample quality inside this square to be as homogeneous as possible. Any variations in the sample uniformity generate variations in $\rho(\phi)$ and $\rho_T(\phi)$. More importantly, there is a profound question on whether domains with different nematic directors form in the nematic phase, like magnetic domains form in ferromagnetic materials. The significant "noise" (deviation from the angular oscillations) in $\rho(\phi)$ and $\rho_T(\phi)$ by the sunbeam method in Figs. 2(e) and 2(f) could be a reflection of the nematic domains distributed across the macroscopic 10 mm × 10 mm space. In contrast, the "noise" in $\rho(\phi)$ and $\rho_T(\phi)$ by the ARR method is remarkably low [Figs. 2(c) and 2(d)] compared to the sunbeam method. The main factor for this significant reduction of the "noise" is the signal from the ARR method is much more local and is averaged only on the area of the small cross section in Fig. 1. This indicates that the nematic domain may be at play. For future studies, the ARR method enables us to fabricate a series of patterns shown in Fig. 1 on the same film and to study spatial variations of the nematicity in search for the nematic domains. Meanwhile, the improved sensitivity by the ARR method also lays down the foundation for studies on the nematic fluctuations, e.g., Goldstone mode or Higgs mode.

The ARR method is also a solution to the measurement of electronic nematicity in bulk crystals. To measure $\rho(\phi)$ and $\rho_T(\phi)$ of bulk crystals, the fabrication of Hall bars along different orientations [27] can be done by focused ion beam but it requires a large bulk crystal, which is very difficult to grow for some materials, and a significant amount of etching time and effort. Similar to the sunbeam method, this also demands a high homogeneity of the bulk crystal. In contrast, the ARR method only needs a sample dimension of 200 μm × 200 μm (which can be shrunk further if needed) so it can be applied even to crystals with small dimensions.

IV. CONCLUSIONS

In summary, by tuning $\boldsymbol{J_x}$ and $\boldsymbol{J_y}$ to continuously rotate the $\boldsymbol{J}$ vector in plane, we substantially reduced the extrinsic effects due to film inhomogeneity and measured the director and amplitude of electronic nematicity with an unprecedented precision. This improvement, we believe, has the potential to propel research progress of identifying more materials with electronic nematicity and deepen our understanding of the underlying mechanisms of electronic nematicity.

ACKNOWLEDGMENTS

This work was supported by the National Natural Science Foundation of China (Grant No. 12174318), the Foundation of Westlake University, and the Westlake Multidisciplinary Research Initiative Center Award (Grant No. MRIC20210102). We acknowledge the assistance provided by the Westlake Center for Micro/Nano Fabrication and the Instrumentation and Service Center for Physical Sciences at Westlake University.

---

[1] E. Fradkin, S. A. Kivelson, M. J. Lawler, J. P. Eisenstein, and A. P. Mackenzie, Annu. Rev. Condens. Matter Phys. **1**, 153 (2010).

[2] S. A. Kivelson, E. Fradkin, and V. J. Emery, Nature (London) **393**, 550 (1998).

[3] J. Zaanen, Z. Nussinov, and S. I. Mukhin, Ann. Phys. **310**, 181 (2004).

[4] D. H. Lu, D. L. Feng, N. P. Armitage, K. M. Shen, A. Damascelli, C. Kim, F. Ronning, Z.-X. Shen, D. A. Bonn, R. Liang, W. N. Hardy, A. I. Rykov, and S. Tajima, Phys. Rev. Lett. **86**, 4370 (2001).

[5] X. J. Zhou, T. Yoshida, S. A. Kellar, P. V. Bogdanov, E. D. Lu, A. Lanzara, M. Nakamura, T. Noda, T. Kakeshita, H. Eisaki, S. Uchida, A. Fujimori, Z. Hussain, and Z.-X. Shen, Phys. Rev. Lett. **86**, 5578 (2001).

[6] Y. Ando, K. Segawa, S. Komiya, and A. N. Lavrov, Phys. Rev. Lett. **88**, 137005 (2002).

[7] M. Abdel-Jawad, M. P. Kennett, L. Balicas, A. Carrington, A. P. Mackenzie, R. H. McKenzie, and N. E. Hussey, Nat. Phys. **2**, 821 (2006).

[8] J. Wu, A. T. Bollinger, X. He, and I. Božović, Nature (London) **547**, 432 (2017).

[9] J. Wu, A. T. Bollinger, X. He, and I. Božović, J. Supercond. Novel Magn. **32**, 1623 (2019).

[10] J. Wu, A. T. Bollinger, X. He, G. D. Gu, M. Hu, M. P. M. Dean, I. K. Robinson, and I. Božović, J. Supercond. Novel Magn. **33**, 87 (2020).

[11] L. Li, N. Alidoust, J. M. Tranquada, G. D. Gu, and N. P. Ong, Phys. Rev. Lett. **107**, 277001 (2011).

[12] M. J. Lawler, K. Fujita, J. Lee, A. R. Schmidt, Y. Kohsaka, C. K. Kim, H. Eisaki, S. Uchida, J. C. Davis, J. P. Sethna, and E.-A. Kim, Nature (London) **466**, 347 (2010).

[13] L. Zhao, C. A. Belvin, R. Liang, D. A. Bonn, W. N. Hardy, N. P. Armitage, and D. Hsieh, Nat. Phys. **13**, 250 (2017).

[14] A. Mukherjee, J. Seo, M. M. Arik, H. Zhang, C. C. Zhang, T. Kirzhner, D. K. George, A. G. Markelz, N. P. Armitage, G. Koren, J. Y. T. Wei, and J. Cerne, Phys. Rev. B **102**, 054520 (2020).

[15] J. Kokalj and R. H. McKenzie, Phys. Rev. Lett. **107**, 147001 (2011).

[16] R. A. Borzi, S. A. Grigera, J. Farrell, R. S. Perry, S. J. S. Lister, S. L. Lee, D. A. Tennant, Y. Maeno, and A. P. Mackenzie, Science **315**, 214 (2007).

[17] J. Wu, H. P. Nair, A. T. Bollinger, X. He, I. Robinson, N. J. Schreiber, K. M. Shen, D. G. Schlom, and I. Božović, Proc. Natl. Acad. Sci. USA **117**, 10654 (2020).

[18] R. M. Fernandes, A. V. Chubukov, and J. Schmalian, Nat. Phys. **10**, 97 (2014).

[19] Q. M. Si, R. Yu, and E. Abrahams, Nat. Rev. Mater. **1**, 16017 (2016).

[20] J. H. Wang, Y. S. Wu, X. Zhou, Y. F. Li, B. L. Teng, P. Dong, J. D. He, Y. W. Zhang, Y. F. Ding, and J. Li, Adv. Phys.: X **6**, 1878931 (2021).

[21] F. Ronning, T. Helm, K. R. Shirer, M. D. Bachmann, L. Balicas, M. K. Chan, B. J. Ramshaw, R. D. McDonald, F. F. Balakirev, M. Jaime, E. D. Bauer, and P. J. W. Moll, Nature (London) **548**, 313 (2017).

[22] Y. Cao, D. Rodan-Legrain, J. M. Park, N. F. Q. Yuan, K. Watanabe, T. Taniguchi, R. M. Fernandes, L. Fu, and P. Jarillo-Herrero, Science **372**, 264 (2021).

[23] P. Walmsley and I. R. Fisher, Rev. Sci. Instrum. **88**, 043901 (2017).

[24] J. Stohr and H. C. Siegmann, *Magnetism: From Fundamentals to Nanoscale Dynamics* (Springer, Berlin, 2006), p. 556.

[25] J. E. Villegas, E. M. Gonzalez, M. I. Montero, I. K. Schuller, and J. L. Vicent, Phys. Rev. B **68**, 224504 (2003).

[26] T. T. Wang, S. Dong, C. Li, W. C. Yue, Y. Y. Lyu, C. G. Wang, C. K. Zeng, Z. X. Yuan, W. Zhu, Z. L. Xiao, X. L. Lu, B. Liu, H. Lu, H. B. Wang, P. H. Wu, W. K. Kwok, and Y. L. Wang, Appl. Phys. Lett. **121**, 092101 (2022).

[27] M. D. Bachmann, A. L. Sharpe, G. Baker, A. W. Barnard, C. Putzke, T. Scaffidi, N. Nandi, P. H. McGuinness, E. Zhakina, M. Moravec, S. Khim, M. König, D. Goldhaber-Gordon, D. A. Bonn, A. P. Mackenzie, and P. J. W. Moll, Nat. Phys. **18**, 819 (2022).